

# Morphology Transition with Temperature and its Effect on Optical Properties of Colloidal MoS<sub>2</sub> Nanostructures

Simran Lambora and Asha Bhardwaj\*

Cite This: *ACS Omega* 2023, 8, 27725–27731

Read Online

ACCESS |



Metrics &amp; More

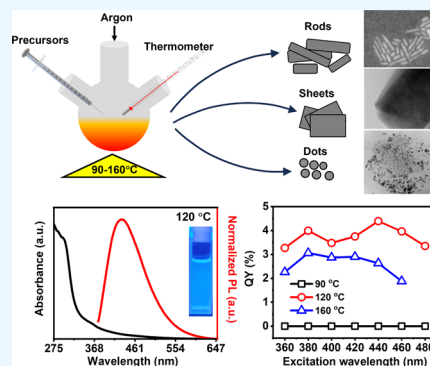


Article Recommendations



Supporting Information

**ABSTRACT:** Morphology plays a crucial role in determining the chemical and optical properties of nanomaterials due to confinement effects. We report the morphology transition of colloidal molybdenum disulfide (MoS<sub>2</sub>) nanostructures, synthesized by a one-pot heat-up method, from a mix of quantum dots (QDs) and nanosheets to predominantly nanorods by varying the synthesis reaction temperature from 90 to 160 °C. The stoichiometry and composition of the synthesized QDs, nanosheets, and nanorods were quantified to be MoS<sub>2</sub> using energy-dispersive X-ray spectroscopy and X-ray photoelectron spectroscopy analyses. A nanostructure morphology transition due to variation in the reaction temperature resulted in a photoluminescence quantum yield enhancement from 0 to 4.4% on increasing the temperature from 90 to 120 °C. On further increase in the temperature to 160 °C, a decrease in the quantum yield to 3.06% is observed. Red-shifts of  $\approx 18$  and  $\approx 140$  nm in the emission maxima and absorption edge, respectively, are observed for the synthesized nanostructures with an increase in the reaction temperature from 90 to 160 °C. The change in the quantum yield is attributed to the change in shape and hence confinement of charge carriers. To the best of our knowledge, microscopic analysis of variation in shape and optical properties of colloidal MoS<sub>2</sub> nanostructures with temperature, explained by a nonclassical growth mechanism is presented here for the first time.



## INTRODUCTION

During the last decade, nanostructured MoS<sub>2</sub> has attracted tremendous attention due to its intrinsic characteristics such as tunable electronic and optical properties, mechanical stability, and photochemical reactivity with applications in field-effect transistors, sensing, energy storage, and catalysis.<sup>1–4</sup> MoS<sub>2</sub> has a layered S–Mo–S structure where the Mo atom is covalently bonded to both S atoms with van der Waals interaction between interlayers. The physical, chemical, electrical, and optical properties of MoS<sub>2</sub> depend on the morphology and size of nanostructures due to quantum confinement effects. MoS<sub>2</sub> in bulk has an indirect band gap ( $\approx 1$  eV), but it transforms into a direct-bandgap material in 2D ( $\approx 1.85$  eV)<sup>5,6</sup> and 0D ( $\approx 4.95$  eV),<sup>7,8</sup> along with enhancement in its electronic, optical, catalytic, and sensing characteristics due to confinement effects, opening a path for optoelectronic and biomedical applications such as optical sensing and bioimaging.<sup>9–17</sup>

Methods such as liquid exfoliation and hydrothermal synthesis have been used to fabricate MoS<sub>2</sub> QDs. However, these synthesis techniques suffer from shortcomings, such as long synthesis durations, low productivity, and small QYs,<sup>17–20</sup> which are avoided in colloidal synthesis.<sup>7,8,12,21,22</sup> Further, the controllability of size and morphology makes the colloidal method a preferred route for nanocrystal synthesis that takes place in three sequential steps of monomer formation, nucleation, and growth of nuclei.<sup>23–27</sup> These monomers can nucleate either through classical condensation, leading to the production of uniform-sized nanoparticles through layer-by-

layer crystal growth, or through nonclassical crystallization, favoring particle attachment by aggregation or oriented coagulation. Nonclassical growth avoids the bottleneck of the classical mechanism by circumventing the constraint of crystal unit cell formation, enabling morphology transition by growth along a specific (low-energy) facet, coalescence, or oriented attachment (OA) of nanoclusters, which is not achievable by the classical mechanism.<sup>28</sup> Control over the size and morphology in the colloidal method can be achieved by varying the reaction temperature, reaction time, capping agents, and precursor concentration.<sup>29–31</sup>

In this article, we report the morphology transition in MoS<sub>2</sub> nanostructures and their optical properties in relation to the reaction temperature ( $T_R$ ). MoS<sub>2</sub> nanostructures with different morphologies, such as QDs, nanosheets, and nanorods, were observed at different  $T_R$ 's ranging from 90 to 160 °C. On increasing the synthesis temperature from 90 to 120 °C, an increase in the number of QDs was observed. Nanorod formation is observed on increasing the  $T_R$  from 120 to 160 °C. Further, optical emission and absorption spectra of these

Received: May 28, 2023

Accepted: July 5, 2023

Published: July 19, 2023



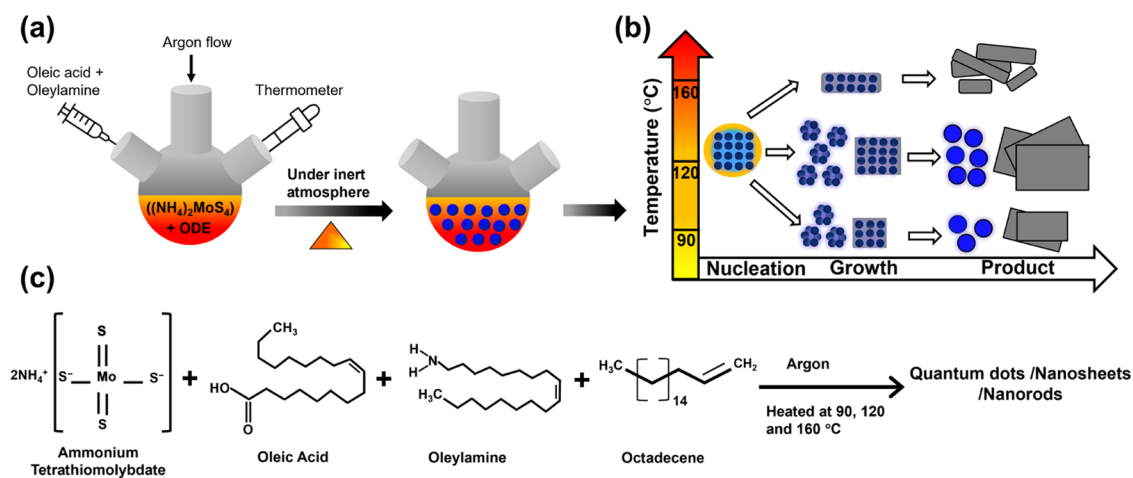


**Figure 1.** Schematic illustrations of the (a) colloidal synthesis of MoS<sub>2</sub> nanostructures using a one-pot heat-up method and (b) possible mechanism of nanostructure formation at different reaction temperatures. (c) Chemical equation depicting the reaction between (NH<sub>4</sub>)<sub>2</sub>MoS<sub>4</sub>, oleic acid, oleylamine, and 1-octadecene to form MoS<sub>2</sub> nanostructures.

chemically synthesized nanostructures are found to be morphology dependent. Compositional analysis performed using X-ray photoelectron spectroscopy (XPS) and Fourier transform infrared (FTIR) spectroscopy show the presence of surface groups as well as MoS<sub>2</sub> formation in the synthesized nanostructures.

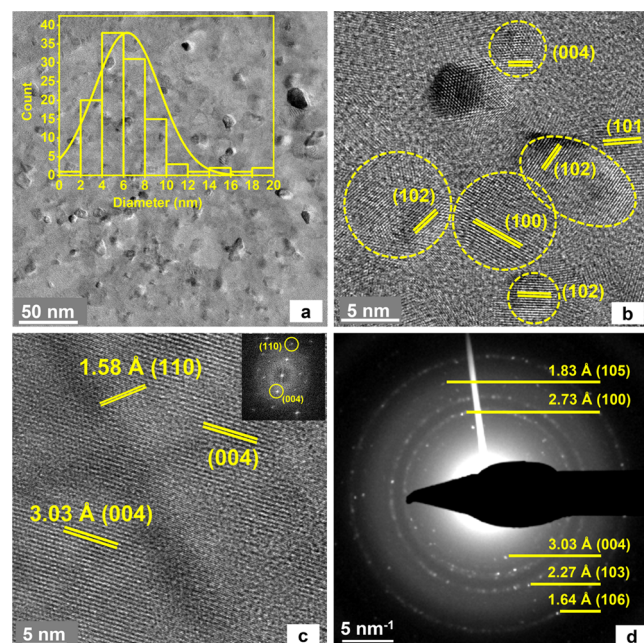
## EXPERIMENTAL SECTION

Figure 1a shows a schematic illustration of the synthesis of MoS<sub>2</sub> nanostructures, wherein a three-neck flask was used to mix all of the reaction precursors. Ammonium tetrathiomolybdate ((NH<sub>4</sub>)<sub>2</sub>MoS<sub>4</sub>) was used as a source of both molybdenum and sulfur elements, with oleylamine (OAm) and oleic acid (OAc) as two capping ligands and 1-octadecene (ODE) as a high-boiling-point non-coordinating solvent. OAm and OAc act as stabilizing agents to quench the dangling bonds on the surface of nanostructures during the growth process. 13 mg of (NH<sub>4</sub>)<sub>2</sub>MoS<sub>4</sub> was mixed with 1 mL of OAc, 3 mL of OAm, and 6 mL of ODE in a three-neck flask. Three mixtures were prepared in three separate flasks and degassed in vacuum for 30 min with continuous stirring. All of the mixed solutions were heated at 90, 120, and 160 °C, respectively, in an argon atmosphere for 25 min. All heated solutions were cooled down to room temperature and then centrifuged at 7000 rpm for 15 min. The obtained precipitates for all three temperatures were dispersed in chloroform to avoid agglomeration of nanostructures. Because of the high pyrolysis temperature of (NH<sub>4</sub>)<sub>2</sub>MoS<sub>4</sub> (≈155 °C), we observe no nanostructure precipitation for  $T_R < 90$  °C, while a very fast reaction occurs for  $T_R > 160$  °C, leading to nonemissive black precipitate formation. The mechanism of resultant nanostructures prepared at 90, 120, and 160 °C is schematically depicted in Figure 1b, showing the formation of nanostructures of MoS<sub>2</sub> with different shapes (nanoparticles, nanosheets, and nanorods), with Figure 1c showing the chemical equation between all reaction precursors.

## RESULTS AND DISCUSSION

Structural analysis of as-synthesized MoS<sub>2</sub> nanostructures fabricated at different  $T_R$ 's was performed by transmission electron microscopy (TEM) and high-resolution transmission electron microscopy (HRTEM) (Titan Themis 300 kV from

FEI). For a reaction temperature of 90 °C, the Gaussian size distribution histogram of MoS<sub>2</sub> QDs was measured for more than 100 particles, and the average particle size was calculated to be ≈6.38 nm in diameter, as evident from the TEM image (inset, Figure 2a). An HRTEM image of these QDs is shown in Figure 2b with the (*hkl*) planes marked. A low  $T_R$  (90 °C) led to a small fraction of monomer formation (<supersaturation state) for nucleation, favoring QDs with a small probability of nanosheet formation. OA among QDs is favored by capping agents (OAc and OAm) that get adsorbed on the nanoparticle surface by hindering the competitive Ostwald



**Figure 2.** (a) TEM image of QDs prepared at  $T_R = 90$  °C, with the size distribution histogram in the inset; HRTEM images showing (b) quantum dots, with the (*hkl*) planes marked and (c) nanosheet with interatomic distances of 3.03 Å (004) and 1.58 Å (110), with the FFT of the scanned area in the inset; (d) SAED pattern recorded for the QDs showing an orientation of QDs along different planes and interatomic distances, with the corresponding (*hkl*) planes marked for all points in the SAED pattern.

ripening (OR) process. QDs formed are not orientation specific, as shown in Figure 2b, depicting the (100), (102), (004), and other planes that may result in polycrystalline sheets through the coalescence process<sup>26</sup> followed by OR, as evident in Figure 2c. The higher surface energy of nanocrystals is responsible for the nonclassical mechanism of aggregation forming attachment along the direction that reduces energy, giving it an orientation as observed in the growth along the (004) and (110) planes in the fast Fourier transform (FFT) pattern of nanosheets (inset, Figure 2c). The polycrystalline nature of nanoparticles is confirmed in the selected-area electron diffraction (SAED) pattern shown in Figure 2d by the presence of the (004), (100), (103), (105), and (106) planes with the interplanar distance corresponding to 2-H MoS<sub>2</sub>, which agrees with the (*hkl*) planes calculated from the HRTEM image.

An MoS<sub>2</sub> nanostructure sample prepared at  $T_R \sim 120$  °C shows the presence of QDs as well as nanosheets (Figure 3a,b). At a higher temperature (120 °C), the number of QDs

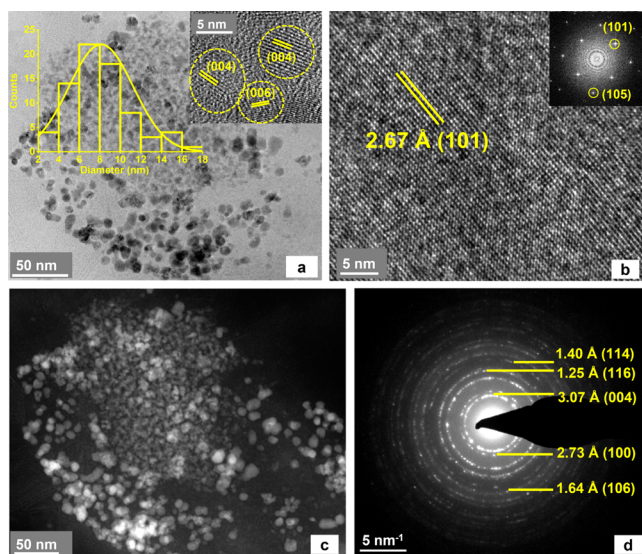


**Figure 3.** (a) TEM image of MoS<sub>2</sub> QDs synthesized at  $T_R = 120$  °C, with the (*hkl*) planes marked in the HRTEM image of QDs and size distribution histogram displayed in the insets. (b) HRTEM of a nanosheet having an interatomic distance of 2.67 Å (101), with the FFT in the inset. (c) Dark-field STEM image of QDs. (d) SAED pattern recorded for MoS<sub>2</sub> QDs showing multiple rings attributed to the polycrystalline nature of the synthesized QDs, with the rings marked with interatomic distances and corresponding (*hkl*) planes.

and the nanosheet sizes formed are much larger as compared to the nanostructures formed at lower temperatures (90 °C). With an increase in the synthesis temperature, the supersaturation (number of monomers) increases, leading to more nucleation followed by growth and thus the precipitation of a larger number of QDs. The size distribution histogram shows the average size of QDs to be  $\approx 8.1$  nm in diameter (inset Figure 3a). An HRTEM image of a polycrystalline sheet formed at 120 °C is displayed in Figure 3b. The thickness of the nanosheet was measured by atomic force microscopy (AFM), and the obtained value was  $\approx 4$  nm. Dark-field scanning transmission electron microscopy (STEM) imaging (Figure 3c) was performed for better contrast images. The SAED pattern (Figure 3d) shows the polycrystalline nature of these QDs leading to the formation of polycrystalline

nanosheets. The interplanar distances calculated using the SAED pattern are in good agreement with the interplanar spacings calculated from HRTEM images, indicating a hexagonal lattice structure of MoS<sub>2</sub> nanostructures.

A time-dependent TEM study of the nanosheet formation clearly shows the synergistic effect of OA and OR to form a sheet, as evident in Figure 4a–e. The growth of two nanoparticles with the same orientation takes place by the Ostwald ripening process followed by coalescence<sup>26</sup> of these two nanoparticles through OA. After coalescence through OA and OR, the final structure forms and grows further by OR, leading to the formation of a nanosheet, as shown in Figure 4e.

On further increasing the reaction temperature to 160 °C, nanorod formation was observed (Figure 5). The energy supplied by a high  $T_R$  increases the monomer formation to the state of high supersaturation, leading to the generation of a large number of nuclei. Based on the experimental results, we hypothesize that OA is highly favored over OR due to the high temperature and fast reaction time, leading to the formation of nanorods, as seen in the HRTEM image of the nanostructure in Figure 5b. OA is corroborated by the growth along the (002) plane with an interatomic distance of  $\approx 6.14$  Å corresponding to MoS<sub>2</sub> (Figure 5b). The average length of these nanorods is  $\approx 21$  nm and the width is  $\approx 5.5$  nm, which is shown in the inset in Figure 5a. The height of nanorods was measured to be  $\approx 60$  nm by AFM. A STEM image showing clear nanorods with very good contrast is displayed in Figure 5c. The SAED pattern shows the presence of three planes (004), (100), and (105) with interatomic spacings 3.07, 2.73, and 1.83 Å, respectively. The proposed mechanism of nanosheet and nanorod formation is shown in Figure 6, wherein the dominance of OR leads to the formation of nanosheets, whereas a dominant OA leads to the formation of nanorods.

Compositional analysis was performed to ascertain the stoichiometry of the formed nanostructures at 90, 120, and 160 °C temperatures. Energy-dispersive X-ray spectroscopy (EDS) measurements recorded on dark-field STEM images, as shown in the Supporting Information, Figure S1, confirm MoS<sub>2</sub> formation with 1:2 (Mo:S) stoichiometry.

The optical properties of the prepared nanostructures were studied by UV–vis and fluorescence spectroscopies. Absorption and PL spectra of nanostructures prepared at different temperatures are shown in Figure 7. On increasing the  $T_R$  from 90 to 160 °C, the Urbach tail red-shifts from 500 to 640 nm. The red-shift in the Urbach tail in the absorption spectra can be explained by the change in the band gap of the nanostructure with changing size due to different confinement effects. Further bandgap calculation using the Tauc plot (Figure S2) revealed a decrease from 4.7 eV at 90 °C to 3.9 eV at 120 °C to 3.67 eV at 160 °C in the synthesized nanostructures. The emission maxima of the fluorescence spectra recorded at an excitation wavelength ( $\lambda_{Ex}$ ) of 360 nm red-shifts by  $\approx 18$  nm with an increase in the  $T_R$  from 90 to 160 °C, as evident in Figure 7. This red-shift in the emission maxima is attributed to an increase in the size of nanostructures and morphology transition. Images of MoS<sub>2</sub> nanostructures dispersed in chloroform were captured upon UV irradiation and are displayed in the inset in Figure 7, where nanostructures prepared at 90 °C show poor emission, while nanostructures prepared at 120 and 160 °C show a strong blue emission. The absolute fluorescence QY was calculated using QuantaPhi-2 Horiba Fluoromax plus spectrometer at different

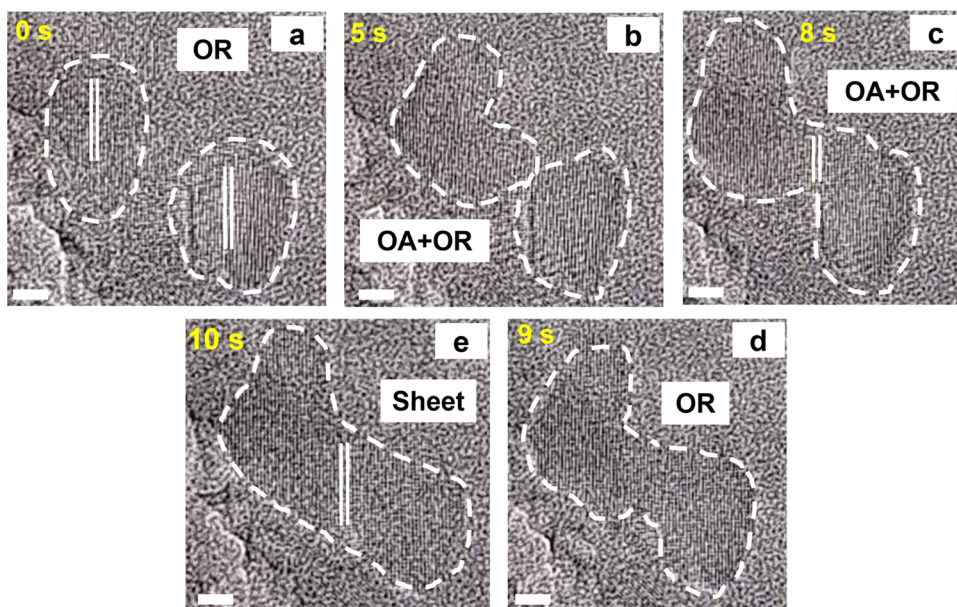


**Figure 4.** HRTEM images of the nanoparticle evolution with increasing reaction time showing the presence of (a) OR at 0 s, (b) OA+OR at 5 s, (c) growth after coalescing with OA+OR at 8 s, (d) growth due to OR at 9s, and (e) final nanosheet formation at 10 s. The scale bar of HRTEM images obtained at 300 KeV is 10 nm.

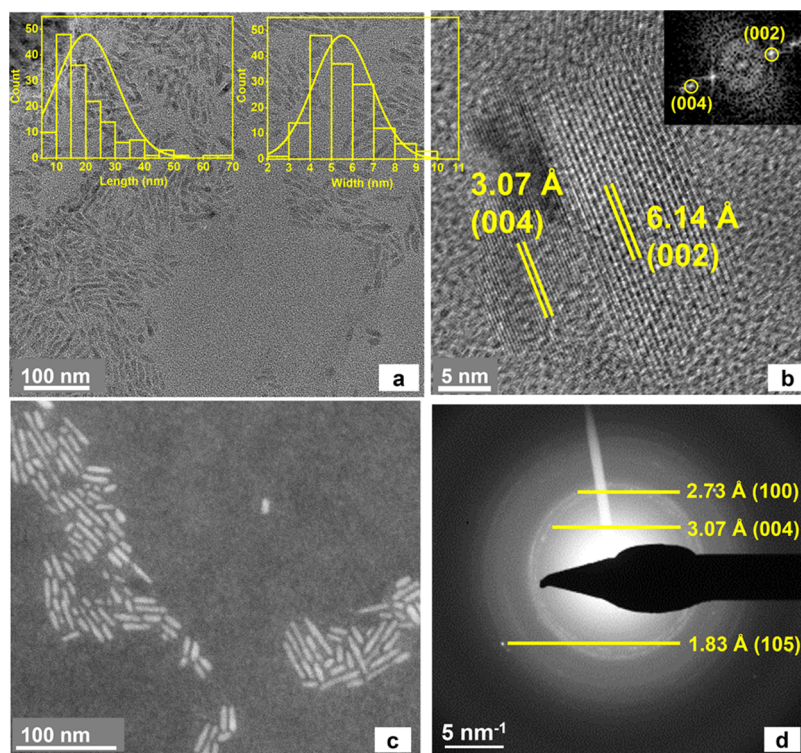


**Figure 5.** (a) TEM image of nanorods, with the size distribution histogram (length and width of nanorods) displayed in the inset. (b) HRTEM image of nanorod growth along the (002) and (004) planes with interplanar distances 3.07 and 6.14 Å, respectively, with the FFT in the inset. (c) Dark-field STEM image of nanorods. (d) SAED pattern of nanorods showing the presence of (100), (004), and (105) (*hkl*) planes. The interatomic distances are marked with their corresponding (*hkl*) planes.

$\lambda_{\text{Ex}}$  values, and the values for all nanostructures synthesized at different  $T_{\text{R}}$ 's are shown in Table 1. Table 1 shows 0 QY for nanostructures prepared at 90 °C, while a maximum QY of 4.4% was observed for nanostructures prepared at 120 °C at  $\lambda_{\text{Ex}} = 440$  nm and 3.06% for those prepared at 160 °C at  $\lambda_{\text{Ex}} = 380$  nm. The change in QY with  $\lambda_{\text{Ex}}$  is attributed to the large size distribution. As observed in TEM images, at a lower

temperature (90 °C), the number of QDs present is lesser than that at higher temperatures (120 °C). A possible reason for the 0 QY value for nanostructures prepared at 90 °C could be greater nonradiative recombination of excitons due to the presence of defects or surface states.<sup>21</sup> With an increase in the reaction temperature to 160 °C, the QY is lower for QDs (120 °C), which is due to the change in the morphology from QDs

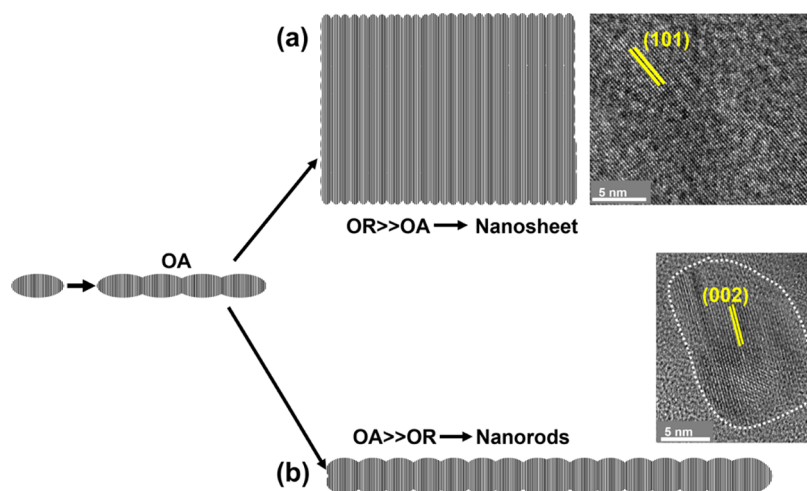


**Figure 6.** Proposed schematic for the formation of nanostructures with different shapes, where nanoparticle attachment takes place through the OA process followed by (a) nanosheet formation when  $OR \gg OA$  and (b) nanorod formation when  $OA \gg OR$ .

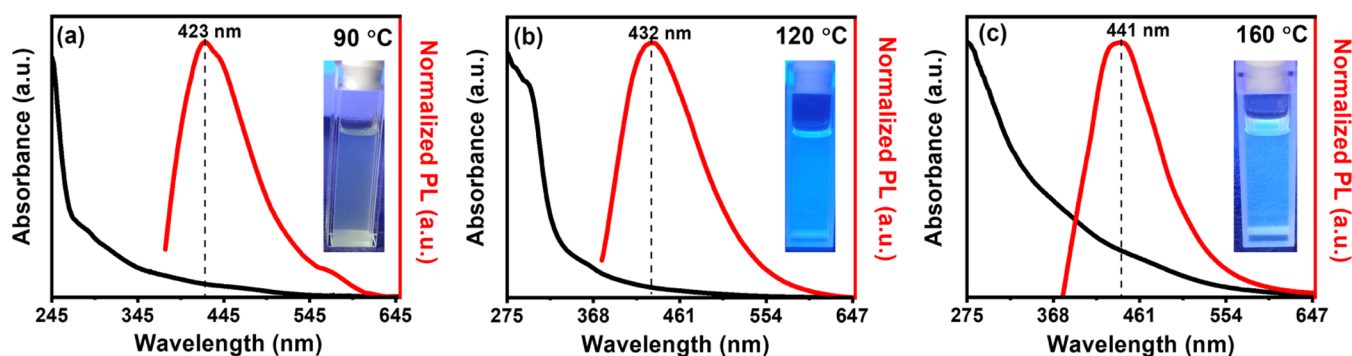


**Figure 7.** Normalized absorption and PL spectra of colloidal  $MoS_2$  nanostructures synthesized at (a) 90, (b) 120, and (c) 160 °C reaction temperatures (insets show images of the corresponding colloidal  $MoS_2$  nanostructures fluorescing under 365 nm UV irradiation).

**Table 1.** QY (%) Variation with  $\lambda_{Ex}$  and Decay Lifetimes at Different  $T_R$  Values

$T_R$ (°C)	$\lambda_{Ex}$ (nm)							lifetime(ns)
	360	380	400	420	440	460	480	
90	0	0	0	0	0	0	0	2.83
120	3.37	3.99	3.48	3.75	4.4	3.96	3.35	2.32
160	2.26	3.06	2.87	2.9	2.63	1.88	1.56	2.03

to nanorods, where charge carriers are poorly confined in comparison to QDs. The variation of QY with  $\lambda_{Ex}$  is shown in Figure S3. The decay lifetime was also measured for nanostructures prepared at all three  $T_R$ 's using a DeltaFlex TCSPC Lifetime Fluorometer with a 350 nm LED source, and the lifetime curves are shown in Figure S3. The average decay lifetimes of nanorods and QDs synthesized at 160 and 120 °C are 2.03 and 2.32 ns, respectively, which are lower than the average lifetime of QDs prepared at 90 °C (lifetime = 2.83 ns); this is attributed to the presence of defect/surface states.<sup>19</sup>

Further information about the surface groups was harnessed by FTIR spectroscopy (Figure 8). FTIR spectra of pure OAm and OAc were also recorded to confirm the presence of surface groups. In Figure 8, the surface groups C=C, C=O, C-N, and C-H confirm the presence of OAc and OAm on the surface of  $MoS_2$  nanostructures synthesized at  $T_R$  values of 90, 120, and 160 °C. Zoomed-in FTIR spectra in the ranges of 4000–1200, 1200–600, and 600–420  $cm^{-1}$  are shown in Figure S4, with all of the bonds marked at their respective

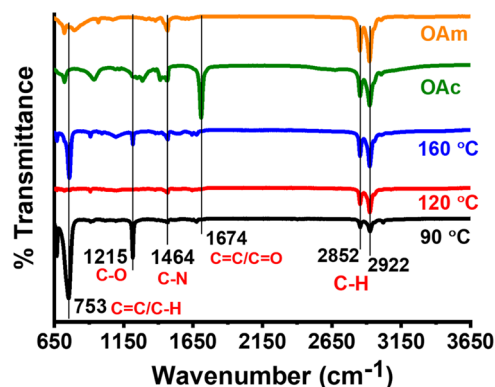


**Figure 8.** Comparison of FTIR spectra of the synthesized nanostructures at varying temperatures of 90, 120, and 160 °C and of the ligands OAm and OAc. The common peaks show the presence of the ligands on the surface of the  $MoS_2$  nanostructures.

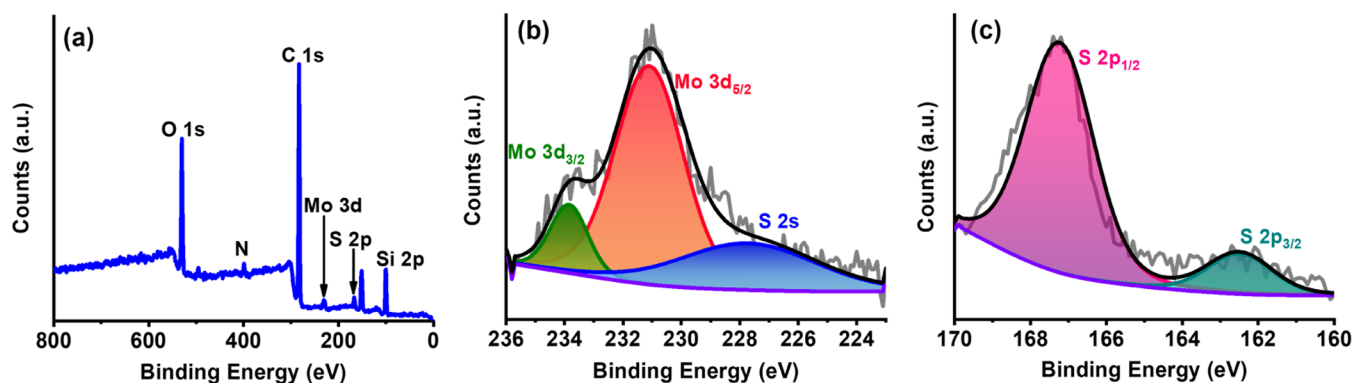


**Figure 9.** (a) Wide-scan XPS spectrum of MoS<sub>2</sub> nanostructures synthesized at 120 °C. (b) Deconvoluted Mo 3d XPS spectrum showing Mo 3d<sub>3/2</sub>, Mo 3d<sub>5/2</sub>, and S 2s peaks. (c) Deconvoluted S 2p XPS spectrum presenting S 2p<sub>1/2</sub> and S 2p<sub>3/2</sub> peaks.

wavenumbers. In Figure S4c, the peak at 537 cm<sup>-1</sup> corresponds to the Mo–S stretching vibration. The FTIR results confirm the presence of surface groups in the synthesized nanostructures.

XPS measurements were performed to confirm the elemental composition of MoS<sub>2</sub> nanostructures synthesized at 120 °C and are shown in Figure 9. The wide-scan XPS spectrum (Figure 9a) shows the presence of Mo and S along with carbon, nitrogen, and oxygen. The presence of C, N, and O elements is due to the capping agents (OAm and OAc). The silicon peak is also observed, which is attributed to the Si substrate used for the measurement over which the colloidal nanostructure solution was drop-cast. The deconvoluted Mo 3d spectrum (Figure 9b) shows the presence of Mo 3d<sub>3/2</sub> and Mo 3d<sub>5/2</sub> positioned at 233.9 and 231.1 eV, respectively. These peaks are blue-shifted in comparison to the bulk MoS<sub>2</sub> (3d<sub>3/2</sub> ≈ 230 eV and 3d<sub>5/2</sub> ≈ 233 eV) by an order of ≈ 2 eV. A similar observation was also made for the deconvoluted S 2p spectrum. In Figure 9c, S 2p<sub>1/2</sub> and S 2p<sub>3/2</sub> peaks are positioned at 167.3 and 162.5 eV, respectively, which are also blue-shifted in comparison to the bulk MoS<sub>2</sub> in which S 2p<sub>1/2</sub> and S 2p<sub>3/2</sub> peaks appear at ≈ 162.9 and ≈ 164.1 eV, respectively. The increase in the binding energy values for both Mo and S can be attributed to the quantum confinement effects in the nanostructures.<sup>21</sup>

## CONCLUSIONS

We report for the first time a study on the morphology transition of MoS<sub>2</sub> colloidal nanostructures from QDs to nanosheets to nanorods with a variation in the synthesis reaction temperature from 90 to 160 °C. OA of highly energetic facets of quantum dots leads to nanosheet and nanorod formation via OR. The nanosheet formation has been explained through time-dependent TEM images showing coalescence through OA followed by OR of nanoparticles. The interplanar distances calculated using the SAED pattern match well with the 2-H phase of bulk MoS<sub>2</sub>. The compositional study using EDS and XPS shows the presence of Mo and S elements in the prepared nanostructures. FTIR results confirmed the presence of surface groups such as C=C, C=O, C–N, O–H, N–H, and C–H due to capping ligands and Mo–S due to MoS<sub>2</sub> in the synthesized nanostructures. From the optical characterization, we showed a high emission from quantum dots and nanosheets prepared at 120 °C, with a quantum yield of 4.4%, compared with those synthesized at 90 °C (quantum dots + nanosheets) and 160 °C (predominantly

nanorods). Further studies are ongoing to understand the effects of the synthesis reaction time and precursor concentrations on the morphology and the optical properties of MoS<sub>2</sub> nanostructures at 120 and 160 °C temperatures. The colloidal synthesis of MoS<sub>2</sub> nanostructures paves the way for applications in optoelectronic devices and bioimaging with reduced synthesis time and control over the morphology of nanostructures.

## ASSOCIATED CONTENT

### Supporting Information

The Supporting Information is available free of charge at <https://pubs.acs.org/doi/10.1021/acsomega.3c03478>.

EDS spectra of MoS<sub>2</sub> nanostructures synthesized at 90, 120, and 160 °C, the Tauc plot used to calculate direct band gap using absorbance data, QY dependence on the excitation wavelength, decay lifetime curves for the synthesized nanostructures at 90, 120, and 160 °C reaction temperatures, and zoomed-in ATR-FTIR spectra of nanostructures prepared at 120 °C (PDF)

## AUTHOR INFORMATION

### Corresponding Author

Asha Bhardwaj – Department of Instrumentation and Applied Physics, Indian Institute of Science, Bangalore 560012, India; [orcid.org/0000-0002-7839-2871](https://orcid.org/0000-0002-7839-2871); Email: [asha@iisc.ac.in](mailto:asha@iisc.ac.in)

### Author

Simran Lambora – Department of Instrumentation and Applied Physics, Indian Institute of Science, Bangalore 560012, India; [orcid.org/0000-0002-6244-3371](https://orcid.org/0000-0002-6244-3371)

Complete contact information is available at: <https://pubs.acs.org/10.1021/acsomega.3c03478>

### Notes

The authors declare no competing financial interest.

## ACKNOWLEDGMENTS

The authors thank the MNCF facility at CeNSE, IISc Bangalore, India. They acknowledge ISRO (grant number ISTC/PIA/AB/460) and the Ministry of Electronics and Information Technology (MeitY) (SP/MITO-19-0005.05) for financial support.

## REFERENCES

- (1) Samadi, M.; Sarikhani, N.; Zirak, M.; Zhang, H.; Zhang, H.-L.; Moshfegh, A. Z. Group 6 transition metal dichalcogenide nanomaterials: synthesis, applications and future perspectives. *Nanoscale Horiz.* **2018**, *3*, 90–204.
- (2) Wang, Q. H.; Kalantar-Zadeh, K.; Kis, A.; Coleman, J. N.; Strano, M. S. Electronics and optoelectronics of two-dimensional transition metal dichalcogenides. *Nat. Nanotechnol.* **2012**, *7*, 699–712.
- (3) Bazaka, K.; Levchenko, I.; Lim, J. W. M.; Baranov, O.; Corbella, C.; Xu, S.; Keidar, M. MoS<sub>2</sub>-based nanostructures: synthesis and applications in medicine. *J. Phys. D: Appl. Phys.* **2019**, *52*, No. 183001.
- (4) Musselman, K. P.; Ibrahim, K. H.; Yavuz, M. Research Update: Beyond graphene—Synthesis of functionalized quantum dots of 2D materials and their applications. *APL Mater.* **2018**, *6*, No. 120701.
- (5) Splendiani, A.; Sun, L.; Zhang, Y.; Li, T.; Kim, J.; Chim, C.-Y.; Galli, G.; Wang, F. Emerging photoluminescence in monolayer MoS<sub>2</sub>. *Nano Lett.* **2010**, *10*, 1271–1275.
- (6) Sundaram, R. S.; Engel, M.; Lombardo, A.; Krupke, R.; Ferrari, A.; Avouris, P.; Steiner, M. Electroluminescence in single layer MoS<sub>2</sub>. *Nano Lett.* **2013**, *13*, 1416–1421.
- (7) Lambora, S.; Bhardwaj, A. In *UV Emitting Colloidal MoS<sub>2</sub> Quantum Dots*, Novel Optical Materials and Applications, 2022; pp NoTu4C-3.
- (8) Lambora, S.; Bhardwaj, A. In *Highly Emitting Colloidal MoS<sub>2</sub> Quantum Dots for Optoelectronic Applications*, Proc. of SPIE, 2022; pp 1201007-1.
- (9) Ayari, A.; Cobas, E.; Ogundadegbe, O.; Fuhrer, M. S. Realization and electrical characterization of ultrathin crystals of layered transition-metal dichalcogenides. *J. Appl. Phys.* **2007**, *101*, No. 014507.
- (10) Kwon, H.; Garg, S.; Park, J. H.; Jeong, Y.; Yu, S.; Kim, S. M.; Kung, P.; Im, S. Monolayer MoS<sub>2</sub> field-effect transistors patterned by photolithography for active matrix pixels in organic light-emitting diodes. *npj 2D Mater. Appl.* **2019**, *3*, No. 9.
- (11) Liu, Q.; Hu, C.; Wang, X. A facile one-step method to produce MoS<sub>2</sub> quantum dots as promising bio-imaging materials. *RSC Adv.* **2016**, *6*, 25605–25610.
- (12) Lin, H.; Wang, C.; Wu, J.; Xu, Z.; Huang, Y.; Zhang, C. Colloidal synthesis of MoS<sub>2</sub> quantum dots: size-dependent tunable photoluminescence and bioimaging. *New J. Chem.* **2015**, *39*, 8492–8497.
- (13) Gao, D.; Si, M.; Li, J.; Zhang, J.; Zhang, Z.; Yang, Z.; Xue, D. Ferromagnetism in freestanding MoS<sub>2</sub> nanosheets. *Nanoscale Res. Lett.* **2013**, *8*, No. 129.
- (14) Perumal Veeramalai, C.; Li, F.; Guo, T.; Kim, T. W. Highly flexible memristive devices based on MoS<sub>2</sub> quantum dots sandwiched between PMSSQ layers. *Dalton Trans.* **2019**, *48*, 2422–2429.
- (15) Mishra, H.; Singh, S. K.; Singh, V. K.; Singh, J.; Srikrishna, S.; Srivastava, A. Highly stable and bio-compatible luminescent molybdenum disulfide quantum dots for imaging of alimentary canal in *Drosophila*. *J. Lumin.* **2018**, *202*, 111–117.
- (16) Dong, H.; Tang, S.; Hao, Y.; Yu, H.; Dai, W.; Zhao, G.; Cao, Y.; Lu, H.; Zhang, X.; Ju, H. Fluorescent MoS<sub>2</sub> quantum dots: ultrasonic preparation, up-conversion and down-conversion bioimaging, and photodynamic therapy. *ACS Appl. Mater. Interfaces* **2016**, *8*, 3107–3114.
- (17) Mukherjee, S.; Maiti, R.; Katiyar, A. K.; Das, S.; Ray, S. K. Novel colloidal MoS<sub>2</sub> quantum dot heterojunctions on silicon platforms for multifunctional optoelectronic devices. *Sci. Rep.* **2016**, *6*, No. 29016.
- (18) Xu, S.; Li, D.; Wu, P. One-pot, facile, and versatile synthesis of monolayer MoS<sub>2</sub>/WS<sub>2</sub> quantum dots as bioimaging probes and efficient electrocatalysts for hydrogen evolution reaction. *Adv. Funct. Mater.* **2015**, *25*, 1127–1136.
- (19) Xu, Y.; Yan, L.; Li, X.; Xu, H. Fabrication of transition metal dichalcogenides quantum dots based on femtosecond laser ablation. *Sci. Rep.* **2019**, *9*, No. 2931.
- (20) Gan, Z. X.; Liu, L. Z.; Wu, H. Y.; Hao, Y. L.; Shan, Y.; Wu, X. L.; Chu, P. K. Quantum confinement effects across two-dimensional planes in MoS<sub>2</sub> quantum dots. *Appl. Phys. Lett.* **2015**, *106*, No. 233113.
- (21) Lambora, S.; Bhardwaj, A. Role of dielectric medium on optical behaviour of blue emitting colloidal MoS<sub>2</sub> quantum Dots. *J. Lumin.* **2023**, *255*, No. 119598.
- (22) Lambora, S.; Bhardwaj, A. In *Optimization of Ligand Concentration on the Optical Properties of Colloidal MoS<sub>2</sub> Quantum Dots*, IEEE 12th International Conference Nanomaterials: 2022 IEEE 12th International Conference Nanomaterials: Applications & Properties (NAP), 2022; p NSS06-1.
- (23) Wen, T.; Zhang, X.; Zhang, D.; Li, Y.; Zhang, H.; Zhong, Z. The interplay between monomer formation, nucleation and growth during colloidal nanoparticle synthesis. *J. Mater. Sci.* **2021**, *56*, 15718–15732.
- (24) Baek, W.; Chang, H.; Bootharaju, M. S.; Kim, J. H.; Park, S.; Hyeon, T. Recent advances and prospects in colloidal nanomaterials. *JACS au* **2021**, *1*, 1849–1859.
- (25) Xue, X.; Penn, R. L.; Leite, E. R.; Huang, F.; Lin, Z. Crystal growth by oriented attachment: kinetic models and control factors. *CrystEngComm* **2014**, *16*, 1419–1429.
- (26) Thanh, N. T. K.; Maclean, N.; Mahiddine, S. Mechanisms of nucleation and growth of nanoparticles in solution. *Chem. Rev.* **2014**, *114*, 7610–7630.
- (27) Polte, J. Fundamental growth principles of colloidal metal nanoparticles—a new perspective. *CrystEngComm* **2015**, *17*, 6809–6830.
- (28) Jehannin, M.; Rao, A.; Cölfen, H. New horizons of nonclassical crystallization. *J. Am. Chem. Soc.* **2019**, *141*, 10120–10136.
- (29) Madras, G.; McCoy, B. J. Transition from nucleation and growth to Ostwald ripening. *Chem. Eng. Sci.* **2002**, *57*, 3809–3818.
- (30) Madras, G.; McCoy, B. J. Temperature effects during Ostwald ripening. *The. J. Chem. Phys.* **2003**, *119*, 1683–1693.
- (31) Madras, G.; McCoy, B. J. Temperature effects on the transition from nucleation and growth to Ostwald ripening. *Chem. Eng. Sci.* **2004**, *59*, 2753–2765.